# Characterization of negative temperature coefficient of resistivity in $(Sn_{1-x}Ti_x)_{0.95}Sb_{0.05}O_2$ ($x \leq 0.1$) ceramics

**Yu Zhang · Yiwen Wu · Hong Zhang · Wenhao Chen · Gaomin Wang · Zhicheng Li**

**Abstract** Sb-doped $SnO_2$-based ceramics substituted by a trace of titanium, $(Sn_{1-x}Ti_x)_{0.95}Sb_{0.05}O_2$ ($x \leq 0.1$), were prepared through a wet chemical process polymerized with polyvinyl alcohol. The phase component and related electrical properties of the ceramics were investigated. The results show that all the ceramics have the tetragonal rutile-type $SnO_2$ crystalline lattice and show typical effect of negative temperature coefficient (NTC) of resistivity. The room-temperature resistivities and NTC material constants can be adjusted widely by changing the Ti content in the ceramics. The investigations by analyzing the electrochemical impedance spectra at various temperatures show that both grain effect and grain-boundary effect contribute to the NTC feature of the ceramics. The conduction mechanisms combining the electron-hopping model and band conduction are proposed for the NTC effect in the ceramics.

## 1 Introduction

Thermistors with an effect of negative temperature coefficient (NTC) of resistivity are extensively applied in industrial and domestic devices for temperature measurement, automatic control, temperature compensation and voltage stabilization, owing to their high sensitivity and reliability [1]. Traditional NTC ceramic thermistors are composed of transition-metal compounds with the spinel structure such as Mn–Ni–O, Ni–Cu–Mn–O and Mn–Co–Ni–O systems, etc. [2–5]. The applications of these transition-metal NTC compounds are limited at temperatures below 200 °C for the relaxation of the crystal structure at higher temperatures [6, 7]. Therefore, some new types of NTC thermistors have been developed for various applications [8–11].

As one typical semiconductor system, $SnO_2$-based materials have been of tremendous interest for the applications in various fields, e.g., solar cells, gas sensors, Li-ion batteries, etc. [12–14]. Semiconducting feature based on $SnO_2$ is widely used because its conductivity can be facilely adjusted by adding dopants such as $Sb_2O_3$, CuO, $Cr_2O_3$ and $In_2O_3$ [15–18]. The influence of Sb concentration on the electrical properties of the antimony-doped tin oxide (ATO) ceramics was discussed by Saadeddin et al. [19], whose work found that Sb-doped $SnO_2$ ceramics displayed a high electrical conductivity and had non-temperature-sensitive resistivities from 4.2 K to room temperature. On the other hand, recent work showed that ATO ceramics with various sintering aids possess a typical NTC effect above room temperature, and that the room-temperature resistivities ($\rho_{25}$) and NTC material constants ($B_{25/85}$) are closely associated with the Sb content [20–22]. In order to adjust the $\rho_{25}$ and $B_{25/85}$ based on ATO ($Sn_{0.95}Sb_{0.05}O_2$) with a certain Sb concentration, the NTC characteristics of the $Sn_{0.95}Sb_{0.05}O_2$–$BaTi_{0.8}Fe_{0.2}O_{3-\delta}$ composite ceramics were reported recently [23].

To develop a facile way to adjust the $\rho_{25}$ and $B_{25/85}$ based on ATO ($Sn_{0.95}Sb_{0.05}O_2$), Ti-substitution in ATO and the influence of Ti-ion on the related electrical properties, especially, the NTC effect, were investigated in present work.

Y. Zhang · H. Zhang · W. Chen · G. Wang · Z. Li (✉)
School of Materials Science and Engineering, Central South University, Changsha 410083, Hunan, People's Republic of China
e-mail: zhchli@csu.edu.cn

Y. Wu
Inspection Center of Industrial Products and Raw Materials, Shanghai Entry-Exit Inspection and Quarantine Bureau of the People's Republic of China, Shanghai 200135, People's Republic of China

## 2 Experimental

$(Sn_{1-x}Ti_x)_{0.95}Sb_{0.05}O_2$ (denoted as STSO, $x = 0.01$, 0.02, 0.04, 0.06, 0.08, and 0.10) ceramics were prepared through a so-called steric entrapment synthesis method as following [24, 25]. The appropriate amount of starting materials of metal Sn powder, antimonous oxide ($Sb_2O_3$) and tetrabutyl titanate were weighed according to the stoichiometry of STSO. The starting materials were separately dissolved into dilute nitric acid. Polyvinyl alcohol (PVA) was dissolved in distilled water. Then the dissolved salts and PVA solution were mixed at a ratio such that there was one hydroxyl group of PVA for every cation in solution, resulting in precursor solution. This mixed solution was heated with stirring until a crisp gel was obtained as a result of water evaporation. The crisp gel was ground into a powder and then calcined at 600 °C for 1 h to obtain STSO powder. The sintering aid CuO, with the amount of 2 wt% (weight percentage) of the calcined STSO powders, was added and mixed with the STSO powder to enhance the sinterability. The calcined powders were granulated with polyvinyl alcohol solution and pressed into pellets of 12 mm in diameter and about 3 mm in thickness, which were sintered at 1,250 °C for 2 h. Silver paste was painted on both sides of the sintered pellets and dried at 600 °C to obtain electrodes for later electrical measurements.

The sintered pellets were examined by X-ray diffraction (XRD, Rigaku D/max 2500, Japan) with Cu $K_\alpha$ radiation to identify the phase component. Temperature dependence of resistance ($R$–$T$) was measured by using a resistance–temperature measurement system (ZWX-C, China) in the temperature range of 20–300 °C. Impedance measurements were carried out on an electrochemistry workstation (Gamry Reference 600, USA) in the temperature range of 20–280 °C and frequency range of 1 MHz to 0.1 Hz. The morphology of the sintered pellets was observed with a scanning electron microscope (SEM, FEI Quanta 200) on the fracture surfaces. For the transmission electron microscopy (TEM, FEI Titan $G^2$ 60-300) observation, an ion-milled sample was prepared, and bright-field images and selected area electron diffraction (SAED) patterns were obtained.

## 3 Results and discussion

### 3.1 Phase and microstructure investigation

Figure 1 shows the XRD patterns of the as-sintered STSO ($x = 0.01$ and 0.1) ceramics. Both patterns reveal a tetragonal rutile phase structure with space group of $P4_2/mnm$ (136) according to the PDF card of No. 41-1445, and there is no detectable impurity diffraction peak. These indicate that Sb, Ti and Cu ions substituted into the rutile lattice of $SnO_2$. Meanwhile, a slight peak shift could be detected, compared with the
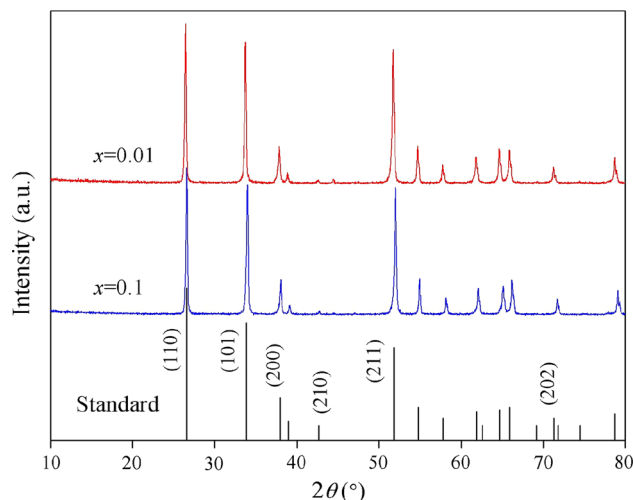


**Fig. 1** X-ray diffraction patterns of the as-sintered $(Sn_{1-x}Ti_x)_{0.95}Sb_{0.05}O_2$ ceramics with $x = 0.1$ and $x = 0.01$, respectively

peaks of the pure $SnO_2$. Refined by MDI Jade 6 program, the lattice parameters were determined to be $a = 4.7233$ Å, $c = 3.1675$ Å for $x = 0.10$, and $a = 4.7399$ Å, $c = 3.1902$ Å for $x = 0.01$. The lattice parameters of both samples are slightly different from the ones of the pure rutile $SnO_2$, $a = 4.7382$ Å, $c = 3.1871$ Å. Due to the different ionic radii in the STSO ceramics, the addition of the smaller ions of $Sb^{5+}$ ($r_{Sb}^{5+} = 0.61$ Å) and $Ti^{4+}$ ($r_{Ti}^{4+} = 0.60$ Å), compared with $r_{Sn}^{4+} = 0.69$ Å, may cause a smaller lattice parameter, while, the introduction of larger ions of $Cu^{2+}$ ($r_{Cu}^{2+} = 0.73$ Å) may slightly enlarge the lattice parameters. Here, the ionic radii were cited from reference [26]. When the amount of Ti is small, $Cu^{2+}$ plays the dominant role in the parameters and increases the lattice parameter, but when the amount of Ti is large enough, the lattice becomes smaller than that of pure rutile $SnO_2$. The variation in lattice parameters is in agreement with calculated values of $a$ and $c$ by Sensato et al. [27].

Figure 2 shows microstructure investigations of an as-sintered $(Sn_{0.94}Ti_{0.06})_{0.95}Sb_{0.05}O_2$ ceramic. Figure 2a, b are the typical SEM images of the fracture surface of the STSO ceramic. Grains are distinctively uniform and densely packed with a low porosity. The grain size is 2–5 μm. Figure 2c, d show typical TEM images and an SAED pattern (upper-right inset in Fig. 2d) taken along $[\bar{2}13]$ from the grain indicated by arrow. The SAED pattern reveals the $SnO_2$-type rutile phase of the STSO ceramics, supporting the XRD analysis that the ceramics are solid solution with a tetragonal rutile phase.

### 3.2 Temperature dependence of resistivity

Figure 3a presents the temperature dependence of resistivity, in Arrhenius plots, of the STSO ceramics with various Ti contents. One can see that the room-temperature
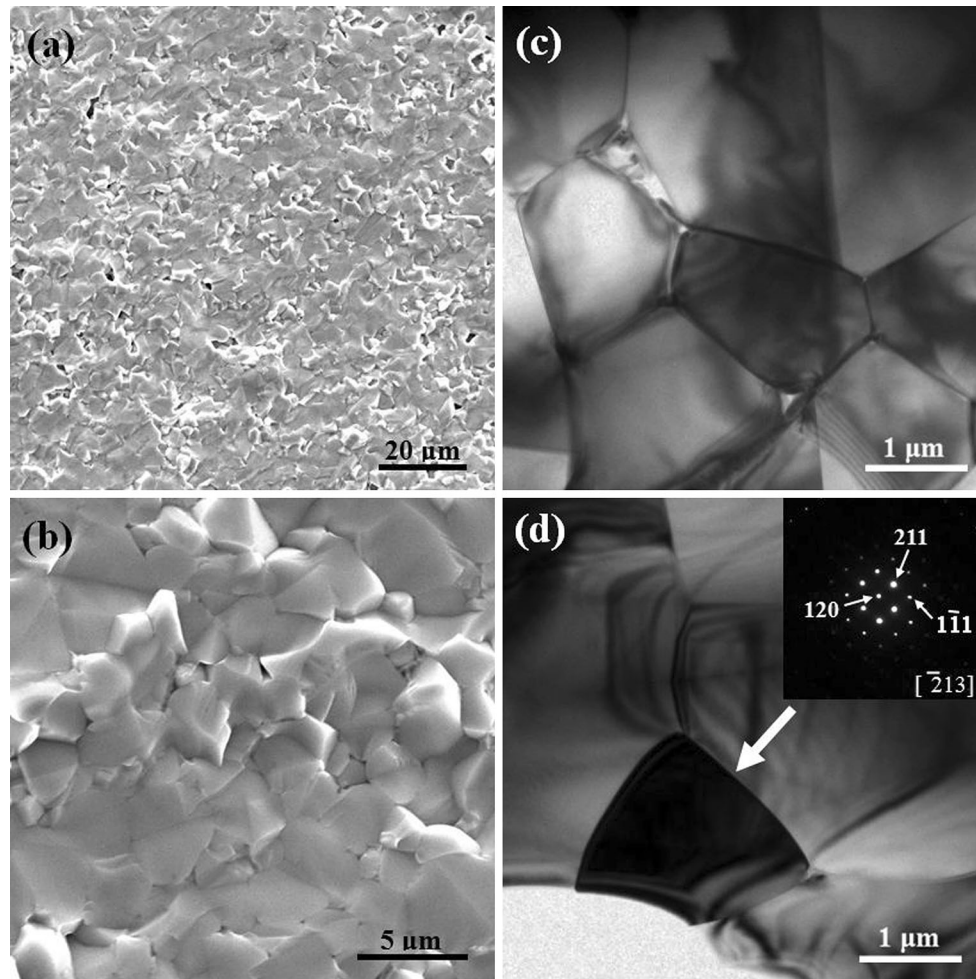
**Fig. 2** Microstructure investigations of as-sintered $(Sn_{0.94}Ti_{0.06})_{0.95}Sb_{0.05}O_2$ ceramic, **a**, **b** SEM images, **c**, **d** typical TEM observations, the *inset* in (**d**) is an SAED pattern from the grain indicated by *arrow*

resistivities of the ceramics increase with the increase of the Ti concentration, and the resistivity of each ceramic decreases as the temperature rises, and that the plots practically preserve linearity when $1,000/T > 2.4$. The STSO ceramics show the typical NTC characteristic. The resistivity–temperature feature complies with the Arrhenius relationship as showed in Eq. (1).

$$\rho = \rho_0 \exp(E_a/k_B T) \tag{1}$$

where $\rho$ is the resistivity, $\rho_0$ the pre-exponential factor, $E_a$ the activation energy of conduction, $k_B$ the Boltzmann constant and $T$ the absolute temperature. For NTC thermistors, $E_a/k_B$ is known as material constant $B$. From an initial temperature $T_0$ to $T$, $B_{T0/T}$ can be calculated using Eq. (2):

$$B_{T_0/T} = \frac{\ln \rho_T - \ln \rho_0}{1/T - 1/T_0} \tag{2}$$

where $\rho_T$ is the resistivity at $T$ and $\rho_0$ is the resistivity at $T_0$. The constant $B$ characterizes the sensitivity to temperature of an NTC thermistor and is related to $E_a$.

The calculated material constants $B_{25/85}$ and resistivities at 25 °C ($\rho_{25}$) of the ceramics are illustrated in Fig. 3b. It can be seen that the $\rho_{25}$ and $B_{25/85}$ of the STSO ceramics can be adjusted in a wide range by adding various contents of Ti. When $x = 0.08$, the constant $B$ value reaches high up to 7,162 K, which is far higher than that of most transition-metal NTC thermistors. For common applications, $B_{25/85}$ is always required from 2,000 to 6,000 K, meaning that STSO ceramics developed in this work are of practical application. Moreover, $\rho_{25}$ increases dramatically with the increase of Ti content ($x$). $B_{25/85}$ keeps growing as well except for $x = 0.1$, where $B_{25/85}$ starts to decline, but it still has a high value of 6,517 K. The addition of titanium increases the utility value of doped $SnO_2$ by providing negative temperature coefficient thermistors with flexible $B$ values, which can be easily controlled through adjusting the content of titanium.

It is obvious that the addition of Ti is responsible for the sharply increasing resistivity of the STSO ceramics at room temperature. Other authors have attributed the effect of Ti
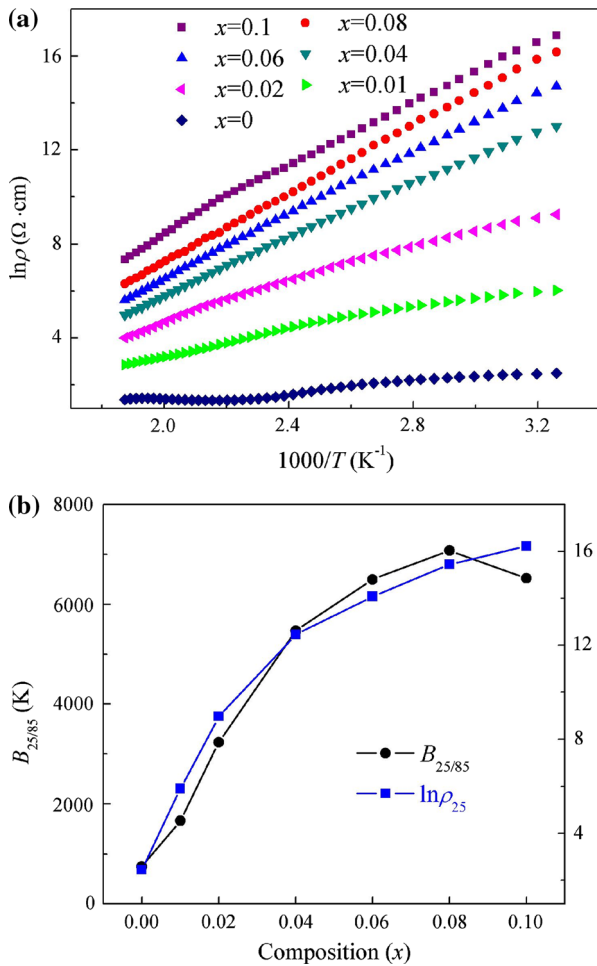
**Fig. 3** Electrical properties of $(Sn_{1-x}Ti_x)_{0.95}Sb_{0.05}O_2$ ceramics, **a** temperature dependence of resistivity, **b** Ti-concentration dependence of material constants ($B_{25/85}$) and room-temperature resistivities ($\rho_{25}$)

to the enhancement of segregation of a second phase, namely segregation of Sb, or to the finely dispersed $TiO_2$ in the bulk [28, 29]. However, based on the analysis of phase and microstructure, the as-prepared ceramics are perfectly single-phased and no such second phases were found. Since the Ti substitution does not affect $Sb^{5+}$ donor concentration in the whole doping range (0–10 %), the increase in $\rho_{25}$ is most likely to be caused by lattice distortion when Sn is substituted by Ti.

### 3.3 Impedance and electric modulus analysis

In order to further investigate the conduction characteristic of the STSO NTC ceramics, AC impedance spectra were employed here. Figure 4 shows a series of Nyquist plots of a STSO ($x = 0.02$) ceramic measured at temperatures from 20
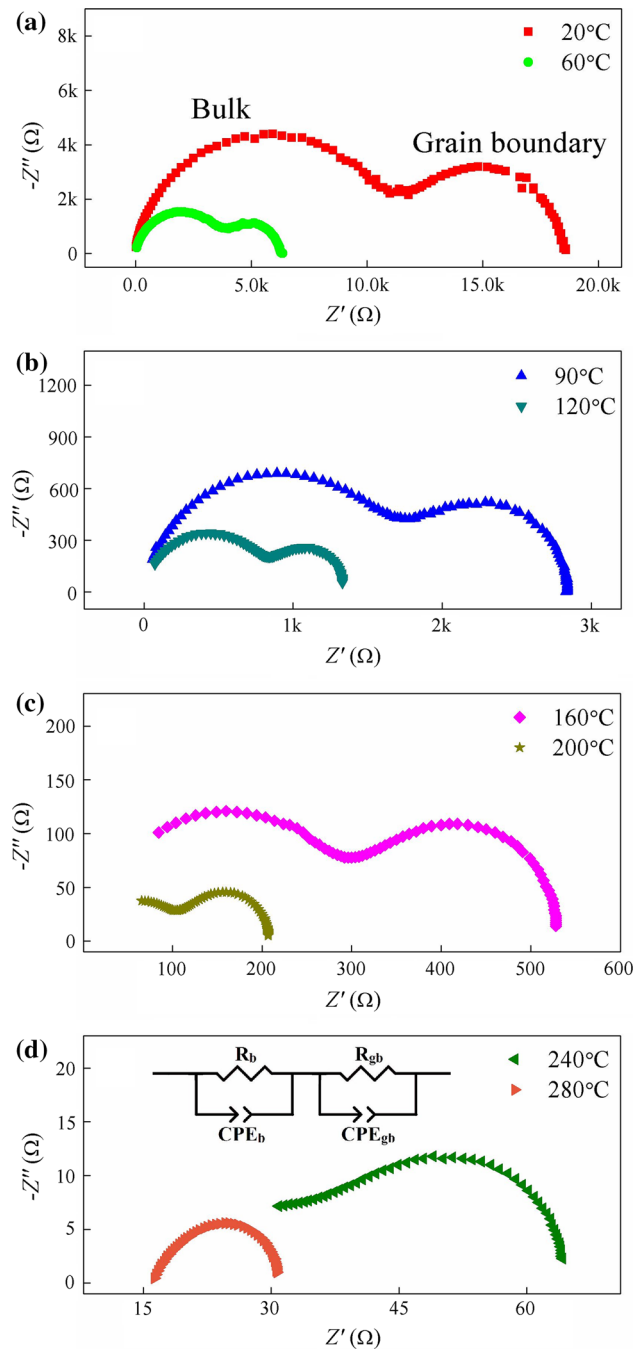


**Fig. 4** Nyquist plots of impedance spectra of $(Sn_{0.98}Ti_{0.02})_{0.95}Sb_{0.05}O_2$ measured at various temperatures, **a** 20 and 60 °C, **b** 90 and 120 °C, **c** 160 and 200 °C, **d** 240 and 280 °C, and an *inset* equivalent circuit model adopted for fitting the impedance spectra

to 280 °C. Two arcs can be observed obviously in the Nyquist plots in the lower temperature region (<160 °C, see in Fig. 4a–c). The high-frequency arc gradually decreased and even disappeared when further rising the temperature (see in Fig. 4c, d), and only one arc can be seen at 280 °C (see in
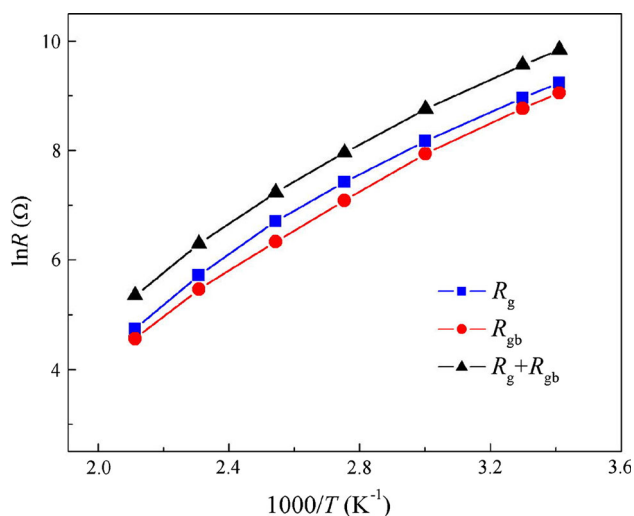
**Fig. 5** Temperature dependence of bulk effect ($R_b$), grain boundary effect ($R_{gb}$) and total resistance ($R_b + R_{gb}$) according to the impedance spectra shown in Fig. 4

Fig. 4d). Generally, the left arc in the higher frequency region corresponds to the response of bulk (grain effect), while the right lower-frequency arc is the response of grain boundary effect [30]. An equivalent circuit (the inset in Fig. 4d) was applied to fit the impedance plots, where $R_b$ and $R_{gb}$ represent the resistance of bulk and grain boundary, respectively, and $CPE_b$ and $CPE_{gb}$ are constant phase elements representing bulk and grain boundary, respectively. The fitted results of the bulk impedance ($R_b$) and grain boundary impedance ($R_{gb}$) are shown in Fig. 5. One can see that $R_b$, $R_{gb}$ and total resistance ($R_b + R_{gb}$) have similar temperature-dependence characteristics, indicating that bulk effect and grain boundary effect contribute comparably to the NTC effect of the STSO ceramics.

The frequency dependence of imaginary part $Z''$ and normalized imaginary part ($Z''/Z''_{max}$) of complex impedances of the STSO ($x = 0.02$) ceramic at different temperatures were analyzed here. The $Z''$-log$f$ plots in Fig. 6a reveal two peaks except for the curve at 240 °C where only one peak at high frequency region is detected due to the limited measuring frequency. The inset plots in Fig. 6a (magnified drawing of $-Z''$ scaled from 0 to 500 Ω) show the peaks more clearly for higher temperatures (120 °C and up). Continuous broadening tendency of the peaks can be observed, indicating a temperature-dependent electrical relaxation behavior in the ceramic. Compared with the Nyquist plots in Fig. 4, it can be deduced that the higher-frequency peak corresponds to the bulk effect, and the lower-frequency peak corresponds to the grain boundary effect. The bulk resistance ($R_b$) and grain boundary
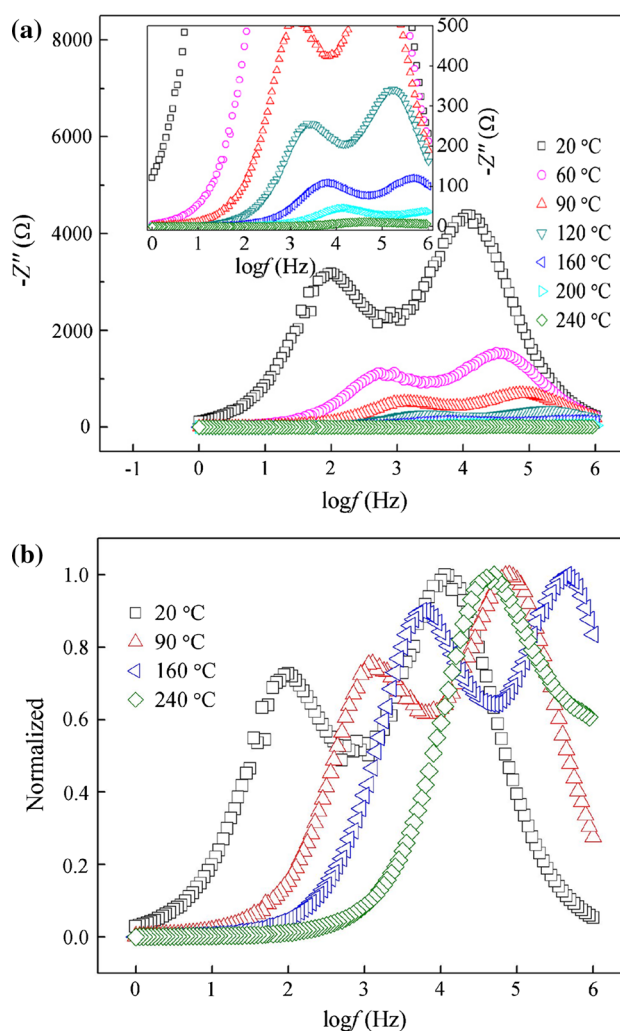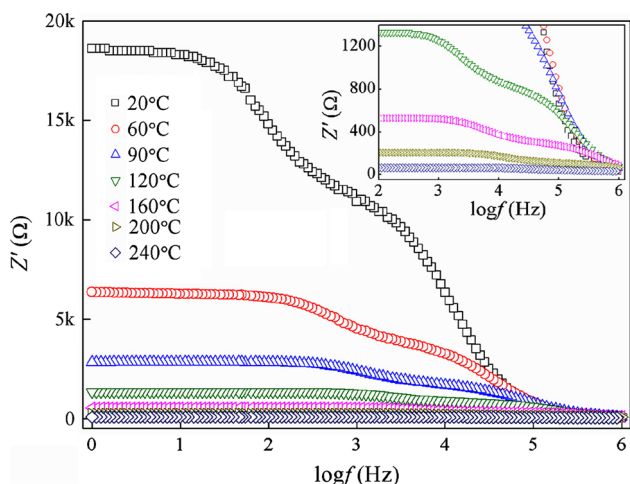


**Fig. 6** Frequency dependence of impedance of $(Sn_{0.98}Ti_{0.02})_{0.95-}$ $Sb_{0.05}O_2$ ceramic at various temperatures, **a** imaginary part ($-Z''$) plots, the *inset* magnified curves at low $-Z''$ from 0 to 500 Ω; **b** normalized imaginary part ($Z''/Z''_{max}$) plots

resistance ($R_{gb}$) are related to the value of $Z''$ governed by Eq. (3):

$$Z'' = R\left[\frac{\omega\tau}{1 + (\omega\tau)^2}\right], \qquad (3)$$

where $R$ is resistance, $\omega = 2\pi f$ is angular frequency, $\tau$ is relaxation time. When $Z''$ reaches a peak, $\omega\tau = 1$; thus, $Z''_{max} = R/2$. This simple relation between $Z''_{max}$ and $R$ helped to calculate $R_b$ and $R_{gb}$, which turned out to be in good accordance with fitted results. The closeness of two peak values also supports the deduction of comparable contribution of bulk effect and grain boundary effect.

Figure 6b shows normalized imaginary part ($Z''/Z''_{max}$) of impedance at some selected temperatures. As temperature

**Fig. 7** Frequency dependence of real part of complex impedance ($Z'$) at various temperatures, the *inset* shows magnified curves at low $Z'$ values and high frequency region from $10^2$ to $10^6$ Hz

rises, the peaks shift towards higher frequency region, indicating a spread of relaxation time which decreases with increasing temperature. The relaxation phenomenon is temperature-dependent and related to certain electrical processes [31].

Figure 7 shows the real part ($Z'$) of the impedance as a function of logarithmic frequency at various temperatures. A plateau appears in each plot at low frequency region, probably resulted from the accumulation of space charges [32]. All curves declines monotonically at higher frequencies to a convergence, indicating the release of space charge, which, consequently, reduces the resistance of the material. The NTC effect is also inferred from the drastic fall of the plateau at low frequencies with rising temperature.

Electrical modulus is another important parameter that is widely used to analyze the conduction feature of semiconductors. To reveal the electrical processes in the ceramics, normalized imaginary part of impedance ($Z''/Z''_{max}$) and electrical modulus ($M''/M''_{max}$) of $(Sn_{0.98-}Ti_{0.02})_{0.95}Sb_{0.05}O_2$ at different temperatures were analyzed as shown in Fig. 8. In each modulus plot, a peak is visible in the lower-frequency region, where the grain-boundary component of $Z''/Z''_{max}$ peak locates. Each of the $M''/M''_{max}$ peak shifts towards higher frequency region, the same as the $Z''/Z''_{max}$ peak does, and remains overlapping with the related grain-boundary $Z''/Z''_{max}$ peak. Supposedly, another $M''/M''_{max}$ peak would turn up at higher frequencies beyond the measuring range. According to the relationship shown in Eq. (4):

$$M'' = \frac{C_0}{C}\left[\frac{\omega\tau}{1+(\omega\tau)^2}\right]. \tag{4}$$

$M''_{max}$ picks out the element with the smallest capacitance since $M''_{max} = C_0/2C$ for that particular element [30]. Since the capacitance of bulk element is smaller than that of grain boundary element, the visible lower frequency $M''/M''_{max}$ peak and the invisible peak are attributed to grain boundary and bulk, respectively.

The overlapping of the lower frequency $M''/M''_{max}$ and $Z''/Z''_{max}$ peaks is the evidence of long-range conduction, or band conduction, caused by the introduction of aliovalent ions such as $Sb^{5+}$. In the STSO ceramics, Sb might have two valence states of $Sb^{3+}$ and $Sb^{5+}$ (primarily $Sb^{5+}$ since sintered in ambient atmosphere), both substituting $Sn^{4+}$ to locate in the octahedral interstices [33]. The doping of Sb significantly reduces the band gap of $SnO_2$, enhancing the charge carriers motion. As the temperature rises, more electrons from valence band are thermally activated and transported out of the potential well thereby contributing to lowering the resistivity of the ceramics (see Eq. (1)). Low frequency makes it possible for charge carriers to move over long distances from one site to a neighboring site.

On the other hand, the mismatch between the higher frequency $M''/M''_{max}$ and $Z''/Z''_{max}$ peaks signifies a localized conduction or hopping conduction. Nobre et al. [34] hypothesized the existence of a transition valence state $Sb^{4+}$ that provides a hopping link between $Sb^{3+}$ and $Sb^{5+}$, such as $Sb^{3+}+Sb^{5+} \rightarrow 2Sb^{4+} \rightarrow Sb^{5+}+Sb^{3+}$. By analyzing the data in Fig. 5, the activation energy $E_a$ for bulk (0.31 eV) was found to be very close to the one for grain boundary (0.33 eV). Not much difference in conduction activation energy exists between bulk and grain boundary. This similar conduction feature in bulk and at grain boundary is corroborative evidence for the deduction that lattice distortion caused by Ti substitution is the reason for the increase in room-temperature resistivity (see Sect. 3.2). The increase in B might be interpreted as an effect of lattice scattering when charge carriers move across bulk and grain boundary, for their similar conductivity properties.

## 4 Conclusions

The Ti-substituted $Sn_{0.95}Sb_{0.05}O_2$ ceramics, $(Sn_{1-x}Ti_x)_{0.95}Sb_{0.05}O_2$ (denoted as STSO, $x = 0.01, 0.02, 0.04, 0.06, 0.08,$ and 0.10), have a tetragonal rutile phase with a space group of $P4_2/mnm$ (136) as that of $SnO_2$. The STSO ceramics show a typical NTC effect, in which the material constant B can be widely adjusted by changing the Ti content, and the constant B value reaches high up to 7,162 K when $x = 0.08$ and is much higher than that of most transition-metal NTC thermistors. The conduction of the STSO ceramics resulted from both grain effect and grain-boundary effect. Two possible

**Fig. 8** Normalized imaginary part of impedance ($Z''/Z''_{max}$) and electrical modulus ($M''/M''_{max}$) at various temperatures, **a** 20, **b** 60, **c** 90, **d** 160, **e** 200, **f** 240 °C
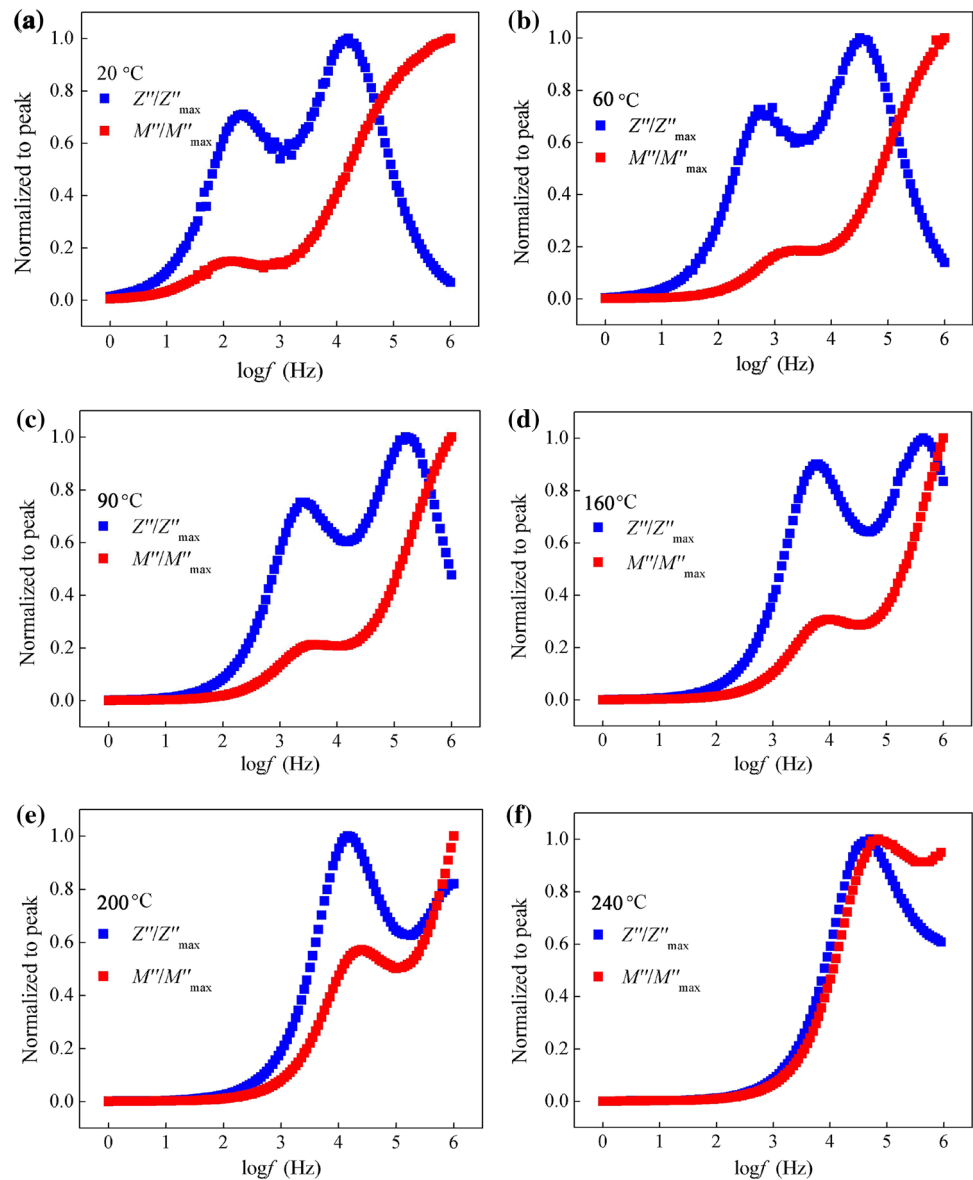


conduction mechanisms are proposed to be the band conduction and hopping conduction models.

## References

1. A. Feteira, J. Am. Ceram. Soc. **92**, 967–983 (2009)
2. E.G. Larson, R.J. Arnott, D.G. Wickham, J. Phys. Chem. Solids **23**, 1771–1781 (1962)
3. F. Fard, Golestani, S. Azimi, K.J.D. Mackenzie, J. Mater. Sci. **22**, 2847–2851 (1987)
4. R. Jadhav, D. Kulkarni, V. Puri, J. Mater. Sci. Mater. Electron. **21**, 503–508 (2010)
5. C.H. Zhao, B.Y. Wang, P.H. Yang, L. Winnubst, C.S. Chen, J. Eur. Ceram. Soc. **28**, 35–40 (2008)
6. X.Q. Li, J. Mater. Sci. **19**, 271–274 (2008)
7. A. Feltz, W. Polzl, J. Eur. Ceram. Soc. **20**, 2353–2366 (2000)
8. K. Park, J. Eur, Ceram. Soc. **26**, 909–914 (2006)
9. K. Park, J. Am. Ceram. Soc. **88**, 862–866 (2005)
10. K. Zakrzewska, Thin Solid Films **391**, 229–238 (2001)
11. J. Wang, H. Zhang, Y. Li, Z. Li, J. Mater. Sci. Mater. Electron. **21**, 811–816 (2010)
12. M.K.I. Senevirathna, P.K.D.D.P. Pitigala, E.V.A. Premal, K. Tennakone, G.R.A. Kumara, A. Konno, Solar Energy Mater. Solar Cells **91**, 544–547 (2007)
13. N. Van Hieu, N.A.P. Duc, T. Trung, M.A. Tuan, N.D. Chien, Sensor. Actuat. B **144**, 450–456 (2010)
14. J. Qian, P. Liu, Y. Xiao, Y. Jiang, Y. Cao, X. Ai, H. Yang, Adv. Mater. **21**, 3663–3667 (2009)

15. S. Zuca, M. Terzi, M. Zaharescu, K. Matiasovsky, J. Mater. Sci. **26**, 1673–1676 (1991)
16. E. Shanthi, V. Dutta, A. Banerjee, K.L. Chopra, J. Appl. Phys. **51**, 6243–6251 (2008)
17. R.S. Niranjan, K.R. Patil, S.R. Sainkar, I.S. Mulla, Mater. Chem. Phys. **80**, 250–256 (2003)
18. W. Chang, S. Lee, C. Yang, T. Lin, Mater. Sci. Eng. B **153**, 57–61 (2008)
19. I. Saadeddin, H.S. Hilal, B. Pecquenard, J. Marcus, A. Mansouri, C. Labrugere, M.A. Subramamina, G. Campet, Solid State Sci. **8**, 7–13 (2006)
20. C.C. Wang, S.A. Akbar, M.J. Madou, J. Electroceram. **2**, 273–282 (1998)
21. G. Li, J. Chen, Z. Hu, C. Liu, Z. Li, H. Zhang, J. Mater. Sci. Eng. **30**(2), 197–201 (2012)
22. Z. Zhang, H. Zhang, J. Wang, W. Li, Z. Li, Electron. Compon. Mater. **28**(6), 56–59 (2009)
23. P. Ouyang, H. Zhang, D. Xue, Z. Li, J. Mater. Sci. Mater Electron. **24**, 3932–3939 (2013)
24. Z. Li, H. Zhang, B. Bergerman, X. Zou, J. Eur. Ceram. Soc. **26**, 2357–2364 (2006)
25. M.A. Gulgun, M.H. Nguyen, W.M. Kriven, J. Am. Ceram. Soc. **82**, 556–560 (1999)
26. R.D. Shannon, Acta Crystallogr. A **32**, 751–767 (1976)
27. F.R. Sensato, R. Custodio, E. Longo, A. Beltrán, J. Andrés, Catal. Today **85**, 145–152 (2003)
28. D.E. Williams, J. Mater. Chem. **9**, 445–450 (1999)
29. W.Y. Chung, D.D. Lee, B.K. Sohn, Thin Solid Films **221**, 304–310 (1992)
30. J.T.S. Irvine, D.C. Sinclair, A.R. West, Adv. Mater. **2**, 132–138 (1990)
31. K. Kumari, K. Prasad, R.N.P. Choudhary, J. Alloy Compd. **453**, 325–331 (2008)
32. S.K. Rout, A. Hussian, J.S. Lee, I.W. Kim, S.I. Woo, J. Alloy Compd. **477**, 706–711 (2009)
33. P. Ouyang, H. Zhang, Y. Wang, W. Chen, Z. Li, Electrochim. Acta **130**, 232–238 (2014)
34. M.A.L. Nobre, S. Lanfredi, Appl. Phys. Lett. **81**, 451–453 (2002)